

# Laser beam welding of deoxidized copper: microstructure investigation and thermodynamic consideration

## Laserstrahlschweißen von desoxidiertem Kupfer: Gefügeuntersuchungen und thermodynamische Betrachtung

H. von Lintel<sup>1,2</sup>, P. Böhlke<sup>2</sup>, H.-G. Wobker<sup>3</sup>, W. Michels<sup>1</sup>, U. Krupp<sup>4</sup>, K. Jahns<sup>1,4</sup>

During the deep-penetration welding of phosphorus deoxidized copper, a multitude of reactions occur which influence the formation of phases inside the welding region. Thereby, the microstructure evolution during laser beam welding depends on the chemical composition of the alloy as well as of the gaseous environment. As a result of reactions in a phosphorus rich copper melt, copper phosphides are formed which are located inside the grains as well as at the grain boundaries. Meanwhile, the formation of phosphorus pentoxide and an uncomplete decomposition of copper-I-oxide to elemental copper and phosphorus pentoxide were identified at the keyhole. Thereby, the decomposition of copper-I-oxide depends on the oxygen concentration. Thus, a complete decomposition of copper-I-oxide to elemental copper and phosphorus pentoxide was observed at the bottom side of the welding region due to a higher oxygen concentration.

**Keywords:** Laser beam welding / copper / precipitation sequence / thermodynamics / microstructure formation

Beim Tiefschweißen eines phosphordesoxidierten Kupfers finden während des Schweißprozesses eine Vielzahl von Reaktionen statt, welche die Phasenbildung innerhalb des Schweißbereiches beeinflussen. In diesem Zusammenhang hängt die Entwicklung des Gefüges von der chemischen Zusammensetzung der Legierung sowie der gasförmigen Umgebung ab. Als Resultat der Reaktionen in der phosphorhaltigen Kupferschmelze bilden sich innerhalb der Schweißnaht Kupferphosphide, die sowohl innerhalb der Körner als auch an den Korngrenzen angeordnet sind. Währenddessen kommt es im Bereich der Dampfkapillare zur Bildung von Phosphorpentoxid und eine unvollständige Zersetzung von Kupfer-I-Oxid zu elementarem Kupfer und Phosphorpentoxid wird identifiziert. Die Zersetzung von Kupfer-I-Oxid ist dabei abhängig von der Sauerstoffkonzentration. Aufgrund der

<sup>1</sup> University of Applied Sciences Osnabrück, Faculty of Engineering and Computer Science, Osnabrück, Federal Republic of Germany

<sup>2</sup> KME Germany GmbH, Osnabrück, Osnabrück, Federal Republic of Germany

<sup>3</sup> KME Special Products GmbH, Osnabrück, Osnabrück, Federal Republic of Germany

<sup>4</sup> RWTH Aachen University, IEHK Steel Institute, Aachen, Federal Republic of Germany

Corresponding author: H. von Lintel, University of Applied Sciences Osnabrück, Faculty of Engineering and Computer Science, Albrechtstraße 30, 49076 Osnabrück, Federal Republic of Germany, E-Mail: heinrich.von-lintel@hs-osnabrueck.de

höheren Sauerstoffkonzentration auf der Unterseite der Schweißnaht zersetzt sich das Kupfer-I-Oxid vollständig zu elementarem Kupfer und Phosphorpentoxid.

**Schlüsselwörter:** Laserstrahlschweißen / Kupfer / Ausscheidungssequenz / Thermodynamik / Gefügebildung

## 1 Introduction

Low-alloyed copper is mainly used due to a good combination of a high heat conductivity and a simultaneously sufficient strength [1]. Therefore, fields of application of such materials are manifold: precipitation-hardenable alloys like CuCr1Zr and CuNi2SiCr may be used, e.g., for electrodes, welding nozzles, or as current-carrying plugs. Phosphorus deoxidized copper which consists only of copper and small amounts of phosphorus is used in building industry as tubes, façade construction and roofing, for heat exchangers, and in electronic applications like in transistors or as material for cables [1, 2]. Welding of phosphorus deoxidized copper is of importance when considering tubing and pipelines, for example as water installations or in apparatus parts for the food, beverage and paper industries [1]. In this context, for the application of tubes, each component has to be joined. Techniques that are commonly used for joining of copper, also in combination with Cu-steel joints, are, e.g., gas metal arc welding and gas tungsten arc welding [3–9]. An alternative is the application of a laser system or hybrid approaches [10–15]. In case of gas metal arc welding and gas tungsten arc welding, an enormous amount of heat is inserted into the large melting zone compared to the laser beam welding [16, 17]. The high heat input with a following long cooling time results in a relatively large heat-affected zone [17, 18]. In contrast, the heat input concentrates on a small area around the laser beam during laser beam welding so that the material is heated up and cooled down much faster [19]. Hence, the resulting heat-affected zone is smaller compared to the heat-affected zone of a gas metal arc welding line and gas tungsten arc welding line, respectively [16–18, 20, 21]. Important to highlight is the fact that with increasing cooling rate, the solidification process of the weld melting pool deviates more and more from the equilibrium conditions. Thus, the microstructure evolution cannot

be described by the equilibrium phase diagrams of copper alloys.

Within manufacturing, the laser beam as a tool represents an efficient technique to precisely join materials compared to conventional welding techniques, like gas metal arc welding or gas tungsten arc welding. Here, the laser beam serves as a heat source for the generation of a welded connection [22, 23]. The mechanism to form a welded joint can be divided in two types. On the one hand, it can be generated via heat conductivity. Therefore, the corresponding welding line is called “heat conduction welding line”. On the other hand, the formation of a keyhole can increase the liquid volume of the melting pool via a multiple reflection of the laser beam inside the keyhole. Hereby, the keyhole is made up of a gaseous phase from the alloying material. Due to the higher welding depth caused by the a multiple reflection of the laser beam, the generated welding line is termed “deep penetration welding line” [22, 24]. However, the welding process of copper via laser beam has two main problems. The first problem involves the low degree of absorption of copper and its alloys. By the use of a conventional red laser with a wavelength of 1030 nm, the degree of absorption for copper is only 3 %, *Figure 1a*. A higher absorption can be achieved by the application of a green laser, where the degree of absorption ( $\lambda_L = 515$  nm) yields to a 15-times higher degree of absorption as compared to the red laser [25, 26]. Furthermore, the heat conductivity of copper is very high and reaches values of about  $400 \text{ W m}^{-1} \text{ K}^{-1}$ , *Figure 1b* [27]. Therefore, the research of laser beam welding of copper and copper alloys concentrates on the expansion of the process limitation and the minimization of welding defects [28–33]. For this purpose, the process limitation complies with the increase of the welding depth. Hence, the formation and the stability of the keyhole during the deep penetration welding are the focus of such research [28–33]. The decisive factor for development of the keyhole is an appropriate ratio between laser power and welding speed.

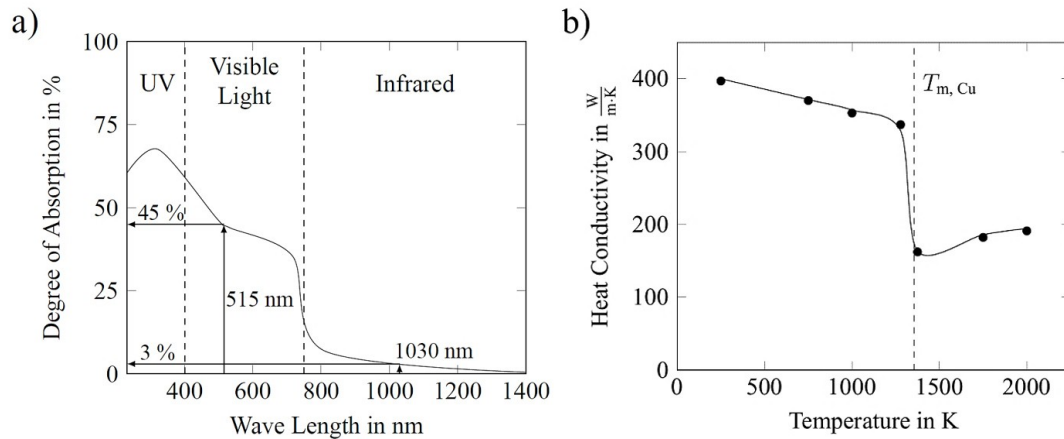


**Figure 1.** a) Degree of absorption of copper as a function of the light wavelength with marked degree of absorption for a conventional red laser ( $\lambda_L = 1030$  nm) with the amount of 3 % and for a green laser ( $\lambda_L = 515$  nm) with 45 % [25], and b) the heat conductivity of copper as a function of the temperature starting by  $400 \text{ W m}^{-1} \text{ K}^{-1}$  at room temperature and a rapid decreasing of the heat conductivity at the melting point of copper below  $200 \text{ W m}^{-1} \text{ K}^{-1}$  [27].

Thereby, for a use of a conventional red laser, a lower laser power limit of 2.2 kW is mentioned in literature for the deep penetration welding process of a 1 mm copper sheet [28]. Moreover, the corresponding welding speed is reported to be smaller than  $10 \text{ mm min}^{-1}$  [29, 30]. Hereby, the stability of the generated keyhole depends on the geometry and the pressure conditions of the gaseous phase. A homogenous shaped keyhole minimizes the risk of welding defects like pores [28, 31, 32]. Hence, a time-dependent function for the laser power is applied to control the shape of the keyhole so that an uncontrolled growth of the keyhole can be avoided [33].

Besides the above described research topics, the microstructure of the joined material and the internal sequence of the welding processes are of significant importance for any technical application. However, the impact of the deep penetration welding concerning the microstructure evolution is not reported in literature so far. Therefore, the present paper aims at a fundamental clarification of the mechanism of microstructure evolution during laser beam welding of copper. For this purpose, deep penetration welding lines are generated and analyzed by means of metallography techniques. This is supported by theoretical analysis of the microstructure by means of thermodynamic calculations.

## 2 Experimental procedure

For the laser beam welding process, deoxidized copper with small amounts of phosphorus is selected. The material consists of at least 99.90 wt. % copper and the phosphorus concentration is in the range between 0.040 wt. % and 0.015 wt. %. For the deep penetration process, a phosphorus deoxidized copper sheet with the dimensions of  $120 \text{ mm} \times 45 \text{ mm} \times 1 \text{ mm}$  is selected. Blind seams with the length of 100 mm are generated.

For performance of the welding process, a Trumpf TruRobot 5020 welding system with a Tru-Disc 3000 laser (3 kW/solid-state laser) was used. The laser power has a time-dependent function over the whole welding process. For the present investigations, the laser power has a sinusoidal function, which can be described according to [33]:

$$P(t) = P_{av} + P_{amp} \cdot \sin(2\pi \cdot f_m \cdot t + \varphi) \quad (1)$$

where  $P_{av}$  is the average laser power,  $P_{amp}$  the amplitude,  $f_m$  the frequency of modulation and  $\varphi$  the phase displacement. The parameters for a laser power modulation include (i) an average laser power of 2.85 kW, (ii) an amplitude of the laser power of 0.15 kW, (iii) a frequency of modulation of 100 Hz, and (iv) a phase displacement of  $90^\circ$ . Furthermore, the laser beam has a spot diameter of 0.4 mm and a welding velocity of  $0.75 \text{ mm min}^{-1}$  is

used. The welding process is performed twice at the same welding line to achieve a deep penetration welding line.

For the metallographic analyses, the welding line was cut as cross-section and hot-embedded in an epoxy-matrix. The section was metallographically ground with silicon carbide paper down to 1000 grit and polished with diamond suspension down to 1  $\mu\text{m}$ . For the observation of the microstructure, a high-resolution scanning-electron-microscope (Zeiss Auriga FEG, with Schottky field emitter gun) in combination with energy dispersive x-ray spectroscopy (EDX) and a light-optical microscope (Zeiss Axio) is used. Furthermore, the surface profile of the welding line is measured with the profile method (tactile measurement, Mar Surf PS 10). The surface profile is recorded at the top and bottom side of the welding line. The measuring direction is perpendicular to the welding line.

### 3 Results

#### 3.1 Observed microstructure of the deep penetration welding line

The deep penetration welding process was applied to a phosphorus deoxidized copper sheets with a thickness of 1 mm, *Figure 2*. Compared to the initial microstructure, the heat-affected zone is characterized by a coarse-grained structure. Starting from the substrate material, the diameter of the grains rises continuously. Thereby, the average grain size (according to DIN EN ISO 643) of the substrate material is 7.4  $\mu\text{m}$  and increases to 120  $\mu\text{m}$  within the heat-affected zone near the welding region. Inside the remelted material, the greatest grain diameter is about 209  $\mu\text{m}$ . Therefore, the changing of the microstructure is divided in three regions in literature: (i) the base metal, the heat-affected zone and the fusion zone [21, 34–37]. In general, the three different regions have a characteristic grain structure. The base metal maintains its initial rolled microstructure. Whereas the heat-affected zone offers an equiaxial grain structure. Inside the fusion zone, the grains offer a columnar structure [34, 37]. Due

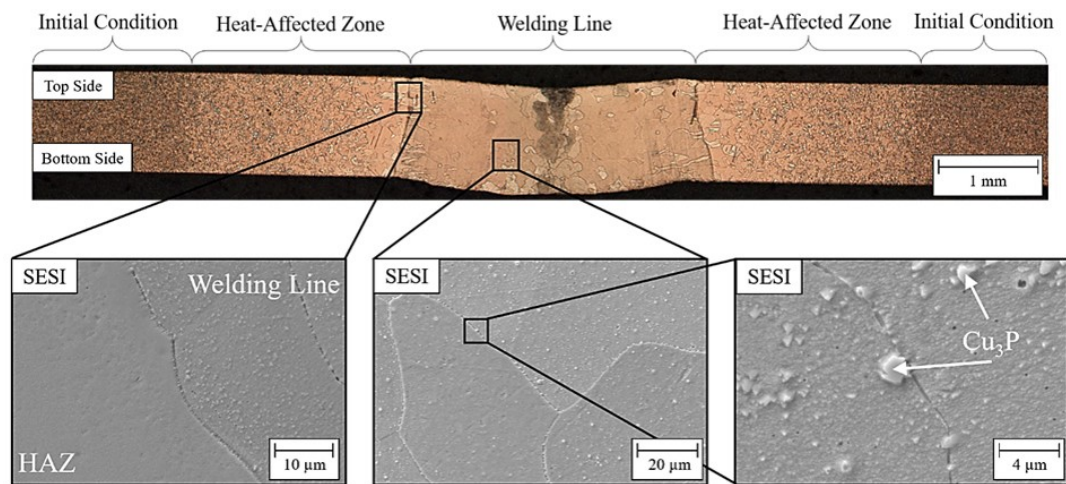


**Figure 2.** Overview image of the cross-section of a welded phosphorus deoxidized copper sheet containing the initial base material, the corresponding heat-affected zone (HAZ) and the welding region with the remolten copper alloy, which are observed with a light optical microscopy (upper image). The base material and the heat affected zone show a homogenous solid solution, where no intermediate phases are formed. However, a grain coarsening occurs inside the heat affected zone. Thereby, the grains grow from 7.4  $\mu\text{m}$  at the base material to 120  $\mu\text{m}$  at the heat affected zone. Furthermore, analytical scanning electron microscopy of the heat-affected zone and the weld region (bottom images) are performed and show copper-phosphides inside the remolten material at the grain boundaries as well as inside the grains, which are detected via darkfield imaging of the optical microscopy and confirmed via energy dispersive x-ray spectroscopy (EDX)-analysis ( $\text{Cu}_{71.1\text{at.}\%}\text{P}_{23.7\text{at.}\%}\text{O}_{5.2\text{at.}\%}$ ).



to the high heat conductivity of copper, the heat-affected zone has a relatively high width. In addition, electron backscattered diffraction (EBSD) measurements show that the crystallographic orientation of the fusion and heat-affected zone can be assumed as random [34]. Moreover, the substrate material as well as the heat affected zone show no formation of intermediate phases so that in this region, a homogenous solid solution is observed.

Furthermore, the microstructure of the remelted region contains small particles, which do not occur at the heat-affected zone or within the initial microstructure. The size of these particles has a value of approximately 2  $\mu\text{m}$ . By energy dispersive x-ray spectroscopy analysis, the chemical composition of the phase was characterized. The result of the analysis shows a copper content of 71.1 at. % and a phosphorus concentration of 23.7 at. %. Furthermore, oxygen is detected with an amount of 5.2 at. %. Consequently, the measured chemical composition indicates that the observed particles can be identified as copper phosphides, which ideal composition include 75 at. % copper and 25 at. % phosphorus. The measured oxygen might result from a thin oxide layer above the sample. The identification of the phases is confirmed via dark field imaging by light optical microscopy. The copper-phosphides precipitates are formed along the grain boundaries as well as inside the grains.

In addition, a deviation of the surface profile is found at the cross-section through the welding line, Figure 3. At the top side, the deviation of the sheet-surface is about 3.5 mm in length and 0.15 mm in depth. At the bottom side, the deviation of the surface profile coincides with the border between the welding line and the heat-affected zone. In this context, the deviation of the surface profile at the top and bottom side is approximately of the same order of magnitude.

The weld microstructure at the top and bottom surface differs from each other with respect to the observed phases. At the surface of the top side, the copper is tarnished within the heat-affected zone, Figure 4. Thus, the tarnished area marks the heat input inside of the heat-affected zone. The darker the coloring of the tarnished area the higher is the heat input. As a consequence, the tarnished area highlights the range of the grain coarsening. Near the welding line is the darkest area so that there are the largest grains. With increasing distance to the

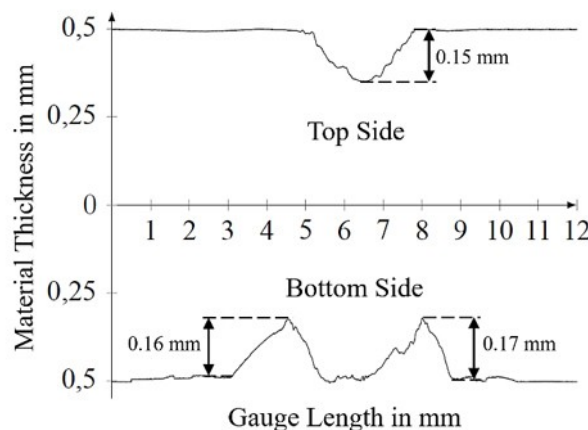


**Figure 3.** Surface profile (cross section through welding line) measured by tactile surface measurement of the top and bottom side of the deep penetration welding line. At the top side of the welding line, a recess of 0.15 mm is caused by the keyhole inside of the welding line. Whereas at the bottom side, the recess with almost the same amount is measured at the heat-affected zone.

welding line, the tarnishing color gets more brighter and the grain coarsening decreases. Furthermore, “dark” phases are formed inside the welding line as well as at the interface to the heat-affected zone. According to analysis via scanning electron microscope, the dark phases can be separated in two parts. The first part is built up of rhombical phase areas of a terraced-shaped structure. The rhombical phase areas are surrounded by a second phase. The energy dispersive x-ray spectroscopy element maps reveal that the rhombical phase areas consist mainly of copper with a concentration of 95.5 at. % and an oxygen content of 4.5 at. %. As a result, the rhombical phase can be assumed as pure copper. The second phase is built up off 23.7 at. % of phosphorus, 71.0 at. % of oxygen and 5.3 at. % of copper. The phase composition indicates that the observed compound can be assumed as phosphorus pentoxide, which ideal composition has a phosphorus content of 28.6 at. % and an oxygen concentration of 71.4 at. %. The measured copper originates from the copper matrix, Figure 4.

The microstructure at the bottom side of the welding lines appears different than the top side, Figure 5. Beside the welding line itself, the surface is covered by a dark scale, which consists of 66.7 at. % of copper and 33.3 at. % of oxygen. Thus, the formed compound was identified as cop-

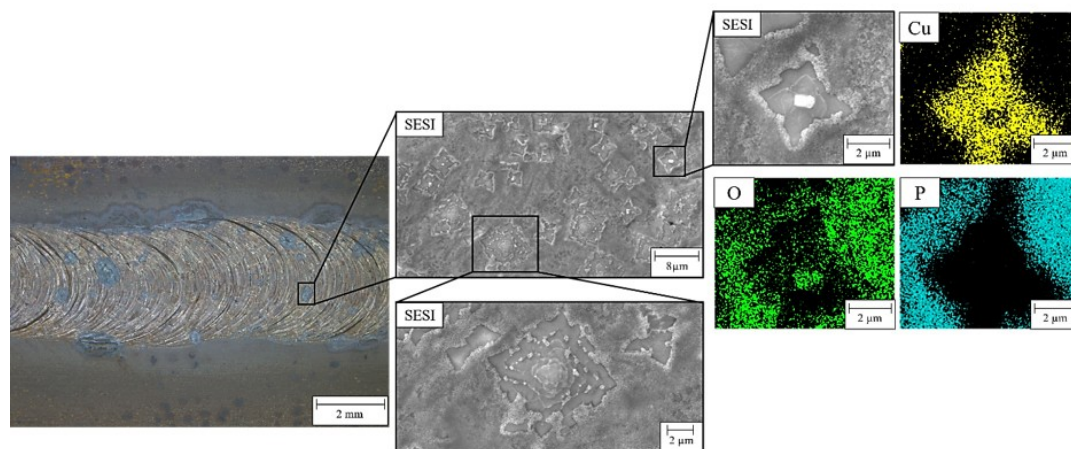


**Figure 4.** Left: Overview of the welding line at the top side via light optical microscopy showing the deep penetration welding line and formed dark precipitations at the welding line, middle: analytical scanning electron microscopy with SESI images of the dark areas. The SESI-images show the arrangement of the dark precipitations with rectangular phases as well as a surrounding phase, right: elemental distribution of precipitations including energy dispersive x-ray spectroscopy (EDX) elemental mapping of copper, oxygen and phosphorus, which indicates the present of copper and copper-oxides inside the rectangular phases and the occurrence of phosphorus-oxide as a surrounding phase.

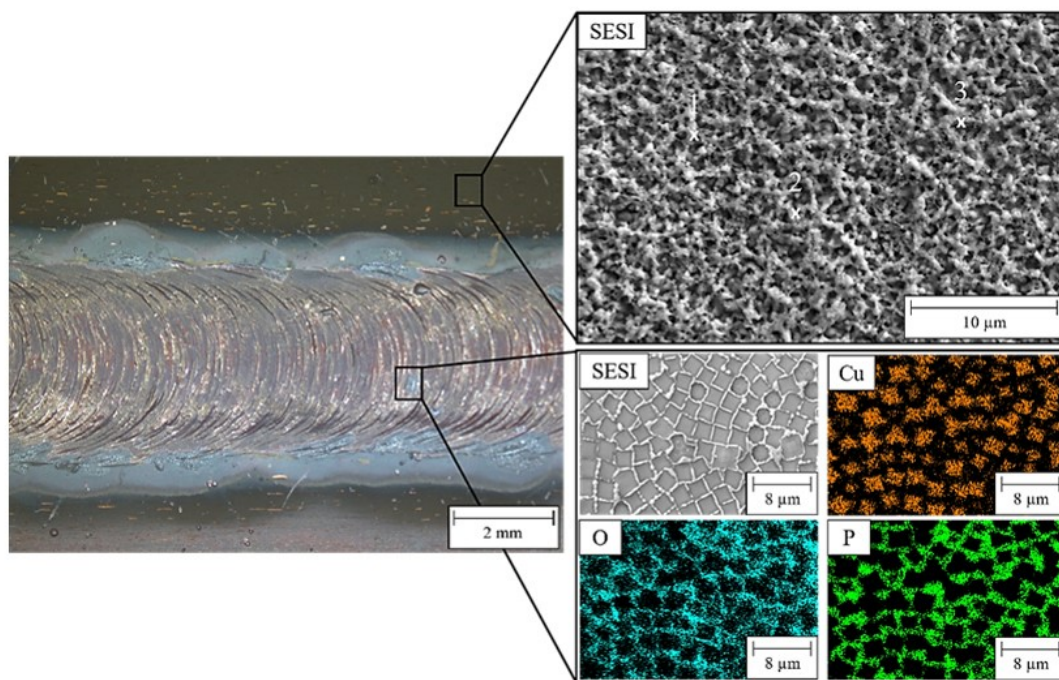


**Figure 5.** Left: Overview of the welding line at the bottom side via light optical microscopy showing the deep penetration welding line and formed silver-shiny precipitations at the welding line as well as a black scale at the transition to the initial phosphorus deoxidized copper sheet, right: analytical scanning electron microscopy with SESI images showing a rectangular arrangement of the silver-shiny precipitations and the black scale. Furthermore, the elemental distribution of precipitations including energy dispersive x-ray spectroscopy (EDX) elemental mapping of copper, oxygen and phosphorus, which indicates the presence of copper for the rectangular phases and the occurrence of phosphorus-oxide as a surrounding phase.

per-I-oxide. Inside the welding line, a silver shiny structure is formed, Figure 5. The detailed scanning electron microscope micrograph of the shiny structure in combination with energy dispersive x-ray spectroscopy (EDX) element mappings illustrates that it consists of two components, i.e., groups of copper rectangles with a content of 97.6 at. %, which are surrounded by a phosphorus-oxygen compound with a phosphorus concentration of 26.6 at. %, 60.3 at. % of oxygen and 13.1 at. % of copper. Assuming that the measured copper content came from the matrix material as well as from the rectangular copper phase, the remaining element concentrations indicate that the surrounded phase is defined as phosphorus pentoxide, Figure 5 right.

### 3.2 Thermodynamic assessment of the phase formation during laser-beam welding

During the deep-penetration welding process, four intermediate phases and one non-metallic oxide is formed. This includes the reaction of copper and oxygen as well as copper with phosphorus. In addition, phosphorus and oxygen can also react with each other. Accordingly, during the laser beam welding procedure of a phosphorus deoxidized copper the chemical compounds of

- copper-I-oxide,
- copper-II-oxide,
- copper phosphide and
- phosphorus pentoxide

have to be taken into consideration. However, the listed phases do not occur *pari passu*. The occurrence of the chemical compounds can be predicted by means of the Gibbs free enthalpy of formation  $\Delta G_f^\ominus$  according to [38]:

$$\Delta G_f^\ominus = \Delta H_f^\ominus - T \cdot \Delta S_f^\ominus \quad (2)$$

In Equation 2,  $\Delta H_f^\ominus$  represents the enthalpy of formation,  $\Delta S_f^\ominus$  the entropy of formation and  $T$  the temperature. For the purpose to clarify the microstructure evolution, the Gibbs free enthalpy of formation is calculated for the listed chemical compounds, Table 1. According to the calculated values, the phosphorus pentoxide phase is the thermodynamically most stable compound. Therefore, the formation of phosphorus pentoxide phase is

**Table 1.** Calculated free Gibb's enthalpy\* of formation of copper-II-oxide (CuO), copper-I-oxide (Cu<sub>2</sub>O), copper-phosphides (Cu<sub>3</sub>P) and phosphorus pentoxide (P<sub>2</sub>O<sub>5</sub>).

Chemical compound	$\Delta H_f^\ominus$ ** in kJ/mol [39, 40]	$\Delta S_f^\ominus$ ** in kJ/(mol K) [39, 40]	$\Delta G_f^\ominus$ in kJ/mol
CuO	−314	0.043	−256.3
Cu <sub>2</sub> O	−333	0.100	−292.5
Cu <sub>3</sub> P	−437	0.119	−383.3
P <sub>2</sub> O <sub>5</sub>	−1505	0.114	−600.0

\* Calculation for 1 mole oxygen/phosphorus

\*\* Values at 298.15 K and 101.3 kPa

dominant for the presence of the elements copper, oxygen and phosphorus. Concerning the intermediate phases, the copper phosphide phase is the most stable one. The copper oxides are generally less stable, while the copper-I-oxide is formed first.

## 4 Discussion

During deep-penetration welding, the phosphorus deoxidized copper sheet is heated up to its vaporization temperature at the top surface within a short time range at the radiation area. It is reported in literature that the vaporization temperature is achieved after 10 μs by using a fiber-laser with a wavelength of 1030 nm and a focal diameter of 100 μm [41]. Due to the localized laser-beam spot, heating and cooling of the material take place approximately in the same amount of period. For the explanation of the microstructure evolution, a simplified schematic sketch of the deep-penetration welding process is used, Figure 6. In this connection, it is assumed that oxygen is present at the bottom as well as at the top side, Figure 6a. The oxygen at the bottom side comes from the air environment. At the top side, the surface of the copper is purged with argon as a shield gas. However, oxygen can appear at a turbulent argon flow in small amounts at small areas as well. Therefore, the key-hole is made up of the gaseous copper, phosphorus and oxygen. In this combination, the inserted phosphorus has different modifications at the gaseous phase. The vaporization temperature of phosphorus is 1073 K. At this temperature, the phosphorus has



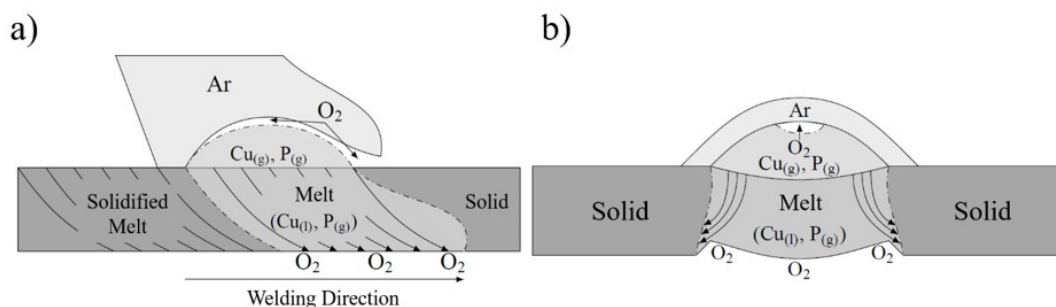


**Figure 6.** Simplified schematic illustration of the a) longitude and b) transverse view of the welding line during the deep-penetration welding process. Both images indicate the present of gaseous copper, oxygen and phosphorus inside the key-hole. Furthermore, the contained elements of the liquid welding line as well as the flow direction of the melt is illustrated.

a trivalent bonding, so that four phosphorus atoms ( $P_4$ ) are arranged tetrahedrally. However, the tetrahedrally phosphorus dissociate continuously towards a bimolecular ( $P_2$ ) structure with increasing temperature. At temperatures exceeding 1473 K, the bimolecular phosphorus structure is the dominant modification. Over 2273 K, the phosphorus occurs atomically [42]. Furthermore, the heating and cooling condition depends on the applied incidence angle, Figure 6a. Therefore, the melt solidifies with almost the same angle as the incidence angle. As a result, the grains of the microstructure exhibit an alignment corresponding to the incidence angle. Additionally, due to the concentrated heat input, the solidified melting pool has a coarse-grained microstructure. Similar results of columnar grain structure were also observed with other laser type (such like fiber laser), a lower incident angle and a smaller focal diameter [34, 37].

The flow behavior of the copper melt and the deviation of surface profile within the welding line can be deduced from the transverse view of the welding line, Figure 6b. Starting from the original top surface, the volume of the melt rises steadily. As a consequence, the width of the welding line extends with increasing depth.

Another aspect of the deep-penetration welding process is the temperature distribution at the welding line. The keyhole is placed directly at the upper surface of the sheet. According to numerical calculations, the temperature field of the gaseous copper has an approximately diameter of 200  $\mu\text{m}$  at a welding speed of 25 m/min, a laser power of 500 W, an incident angle of 18° and a focal diameter of 100  $\mu\text{m}$  after 950  $\mu\text{m}$  [41]. Important to high-

light is that is approximation is only valid for a planar surface [41]. After the development of the keyhole, there is no longer a planar surface at the copper sheet so that a multiple reflection of the laser takes place [34]. The deviation of the planar surface can also be seen at the present results because of a recess after the welding process inside the welding line.

Under the keyhole, the melt is near the vaporization temperature of the material. Therefore, the melting pool is strongly overheated. Once overheating is stopped instantaneously at the bottom side, heat accumulation at this side leads to a temperature increase leading to a reaction of gaseous copper with the surrounding oxygen to copper-I-oxide.

From these considerations, a reconstruction of the observed phases formation and respective microstructure is possible. At first, the phase formation process at the top side of the welding line should be clarified and illustrated, Figure 7. As an initial situation for the phase formation, it is assumed that the keyhole is made up mostly of gaseous copper and phosphorus. The turbulent flow of the argon shield gas alloys penetration of a small amount of oxygen at the keyhole. During this process, the modification of the phosphorus changes to the bimolecular structure of phosphorus after the temperature drops below 2273 K. According to the thermodynamic consideration, the most favorable stable compound is phosphorus pentoxide. When the concentration of phosphorus is not high enough, no more phosphorus pentoxide can be formed. Consequently, phosphorus is ligated completely by the formation of phosphorus pentoxide. Afterwards,



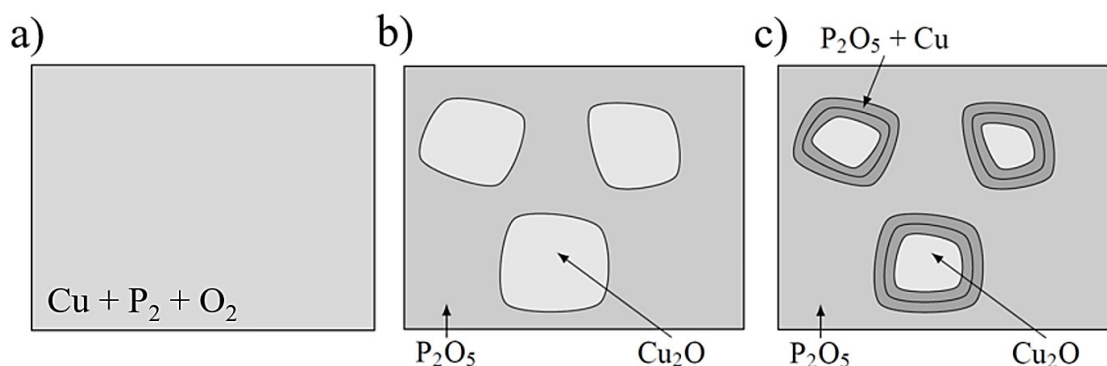
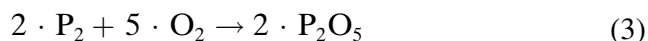


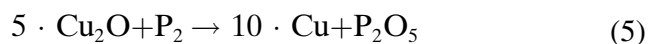
**Figure 7.** Schematic illustration of the phase formation sequence at the top of the welding line, starting from a) the initial situation inside the keyhole, b) the dominated formation of phosphorus pentoxide ( $P_2O_5$ ) and the development copper-I-oxide ( $Cu_2O$ ) particles, and c) the phase structure after the decomposition of the copper-I-oxide in copper and phosphorus pentoxide.

the formation of copper-I-oxide is the most stable reaction. It follows the development of copper-I-oxide particles. The reaction equations for the formation of phosphorus pentoxide and copper-I-oxide can be summarized with following reactions:



The reaction between copper and the molecular phosphorus is suppressed, because the phosphorus serves for the formation of phosphorus pentoxide. Due to the low thermodynamic stability, the formation of copper-II-oxide does not take place.

The formed copper-I-oxide can further react with the remaining bimolecular phosphorus so that a decomposition of the copper-I-oxide particles takes place. At the end of the process, copper-I-oxide and bimolecular phosphorus react to elemental copper and phosphorus pentoxide:



According to the reaction in Equation 3, 5 moles of copper-I-oxide are needed for a complete bimolecular phosphorus decomposition. However, this amount of copper-I-oxide is not available for the chemical conversion. This can be attributed to the fact that most of the oxygen is used for the formation of phosphorus pentoxide (Equation 3). Therefore, the concentration of copper-I-oxide is limited and not sufficient for a complete decom-

position. Hence, the copper-I-oxide particles serve as nucleus for the conversion. The copper and phosphorus pentoxide are formed around the particles and build the rhombical structure, Figures 7, 4.

The center of the welding line is completely depleted in oxygen. Thus, liquid copper and phosphorus build the initial situation, Figure 8. Therefore, the formation of copper phosphide begins immediately, if the phosphorus has the bimolecular phosphorus modification:



It is important to highlight the fact that the copper phosphide has a lower melting temperature than copper. After the process temperature drops below the melting temperature of copper, the behavior of the copper phosphide particles can be described two-fold. On the one hand, the copper phosphide accumulates between the growing copper crystals. On the other hand, copper phosphide particles are overtaken from the solidification front and are placed inside the copper crystals. The copper phosphide particles are solidified at last. The microstructure in the center of the welding exhibits large copper grains with copper phosphide particles occurring inside the grains as well as along the grain boundaries.

At the bottom side of the welding line, the process conditions are similar condition than at the middle of the welding line. The initial situation starts with a copper melt and molecular phosphorous, Figure 9. However, at the surface of the bottom

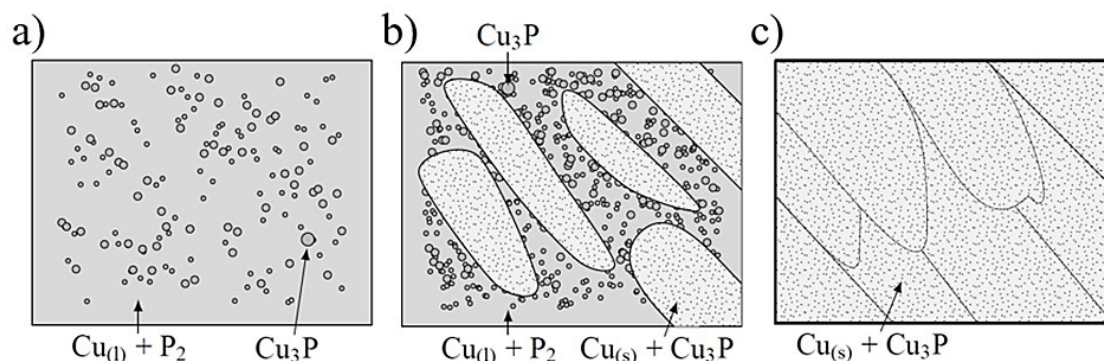


**Figure 8.** Schematic illustration of the microstructure formation inside the welding line, starting from a) the development of copper-phosphides ( $Cu_3P$ ) in the liquid state of copper and the molecular condition of phosphorus, b) the solidification of copper crystals with embedded copper-phosphides particles and liquid copper-phosphides in the interspace of the copper crystals, respectively, and c) completely solidified microstructure of the welding line with copper-phosphides particles inside the grains as well as at the grain boundaries.

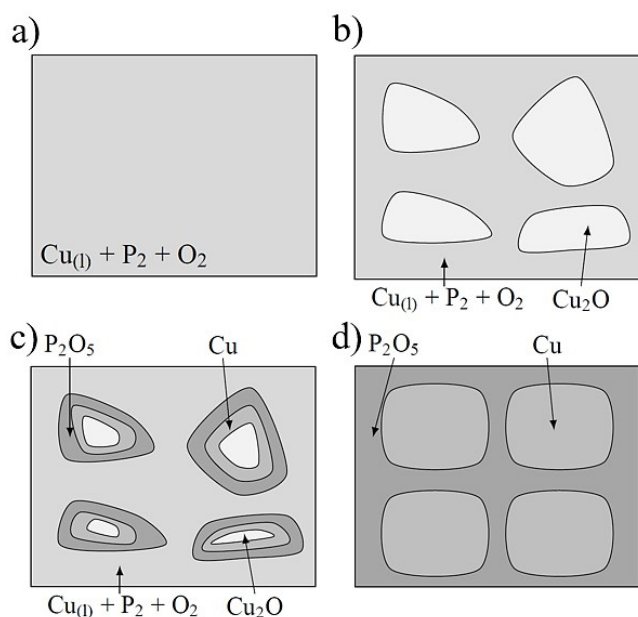


**Figure 9.** Microstructure formation at the surface of the bottom side starting from a) the liquid state of copper with dissolved phosphorus and oxygen, b) the development of closed ceiling of copper-I-oxide, c) beginning decomposition of copper-I-oxide in elemental copper and phosphorus pentoxide, and d) final decomposition of copper-I-oxide in copper and phosphorus pentoxide in a rectangle arrangement.

side, the oxygen concentration is much higher due to the absence of the shielding gas. According to the reaction Equation 3, the formation of phosphorus pentoxide and copper-I-oxide sets in. In contrast to the top side, the oxygen concentration is high enough to allow large-scale formation of copper-I-oxide particles, so that the whole surface in

this area is coated by the oxide. Based on the decomposition reaction in Equation 5, the copper-I-oxide particles react completely to elemental copper and phosphorus pentoxide.

## 5 Conclusions

During the deep-penetration welding of phosphorus deoxidized copper, multiple reactions take place between liquid and gaseous the alloying components with its environment. On the one hand, a formation of segregations mainly of copper phosphides occurs inside the liquid phase. The copper phosphides are placed inside the grains as well as at the grain boundaries can be observed. On the other, reactions inside the keyhole and the bottom side of the welding region form copper-I-oxide and phosphorus pentoxide. Depending on the oxygen concentration, the copper-I-oxide decompose to copper and phosphorus pentoxide.

## Acknowledgement

The financial support of the European Fond for Regional Development (EFRE) is gratefully acknowledged. Open access funding is enabled and organized by project DEAL.

## 6 References

- [1] Deutsches Kupferinstitut, *Cu-DHP: Technical Data Sheet* **2005**.
- [2] D. Becker, *PhD-Thesis*, RWTH Aachen, Germany **2014**.
- [3] Z. Shen, Y. Chen, M. Haghshenas, T. Nguyen, J. Galloway, A.P. Gerlich, *Mater. Charact.* **2015**, 104, 1.
- [4] Y. Zhang, J. Huang, H. Chi, N. Cheng, Z. Cheng, S. Chen, *Mater. Lett.* **2015**, 156, 7.
- [5] M. Velu, S. Bhat, *Mater. Des.* **2013**, 47, 793.
- [6] E. Scutelnicu, M. Iordachescu, D. Iordachescu, *Metalurgia* **2009**, 61, 1.
- [7] S.G. Shiri, M. Nazarzadeh, M. Sharifitabar, M.S. Afarani, *Trans. Nonferrous Met. Soc. China* **2012**, 22, 2937.
- [8] W.H. Minnick, M.A. Prosser, *Gas tungsten arc welding handbook*, Goodheart-Willcox. **2000**.
- [9] M. Gurram, K. Adepur, R. Pinninti, M. Gankidi, *J. Mater. Res. Technol.* **2013**, 2, 238.
- [10] C. Yao, B. Xu, X. Zhang, J. Huang, J. Fu, Y. Wu, *Opt. Laser Eng.* **2009**, 47, 807.
- [11] A. Heider, P. Stritt, A. Hess, R. Weber, T. Graf, *Phys. Procedia* **2011**, 12, 81.
- [12] S. Engler, R. Ramsayer, R. Poprawe, *Phys. Procedia* **2011**, 12, 339.
- [13] A. Heider, J. Sollinger, F. Abt, M. Boley, R. Weber, T. Graf, *Phys. Procedia* **2013**, 41, 112.
- [14] L. Zhang, Q. Bai, J. Ning, A. Wang, J. Yang, X. Yin, J. Zhang, *Mater. Des.* **2016**, 110, 35.
- [15] L. Wang, X. Li, M. Gao, X. Zeng, *J. Manuf. Process.* **2017**, 27, 207.
- [16] A.T. Egbewande, R.A. Buckson, O.A. Ojo, *Mater. Charact.* **2010**, 61, 569.
- [17] L.O. Osoba, O.A. Ojo, *Mater. Sci. Technol.* **2012**, 28, 431.
- [18] G. Padmanaban, V. Balasubramanian, *Opt. Laser Technol.* **2010**, 42, 1253.
- [19] S. Babu, M. Miller, J. Vitek, S. David, *Acta Mater.* **2001**, 49, 4149.
- [20] R. Coelho, A. Kostka, H. Pinto, S. Riekehr, M. Kocak, A. Pyzalla, *Mater. Sci. Eng. A* **2008**, 485, 20.
- [21] B. Oztoprak, E. Akman, M. Hanon, M. Günes, S. Gümüs, E. Kacar, O. Gundogdu, M. Zeren, A. Demir, *Opt. Laser Technol.* **2013**, 45, 748.
- [22] B.S. Yilbas, S. Akhtar, S.Z. Shuja, *Laser forming and welding processes*, Springer **2013**.
- [23] S. Auwal, S. Ramesh, F. Yusof, S. Manladan, *Int. J. Adv. Manuf. Tech.* **2018**, 96, 475.
- [24] P. Ferro, F. Bonollo, A. Tiziani, *Sci. Technol. Weld. Joi.* **2005**, 10, 299.
- [25] K. Sugioka, M. Meunier, A. Piqué, *Laser Precision Microfabrication*, Springer-Verlag Berlin Heidelberg, Berlin, Heidelberg **2010**.
- [26] W. Steen, J. Mazumder, *Laser Material Processing*, Springer-Verlag London, Dordrecht, Heidelberg, New York **2010**.
- [27] A. Blom, P. Dunias, P. van Engen, W. Hoving, J. de Kramer, *Process spread reduction of laser microspot welding of thin copper parts using real-time control*, in: A. Pique, K. Sugioka, P.R. Herman, J. Fieret, F.G. Bachmann, J.J. Dubowski, W. Hoving, K. Washio, D.B. Geohegan, F. Traeger, K. Murakami, *Process spread reduction of laser microspot welding of thin copper parts using real-time control*, SPIE **2003**, 493.
- [28] A. Heider, *PhD-Thesis*, University of Stuttgart, Germany **2018**.
- [29] A. Heß, *PhD-Thesis*, University of Stuttgart, Germany **2012**.
- [30] D. Petring, V. Gonedhany, *J. Laser Appl.* **2010**, 1, 547.
- [31] M. Wahba, M. Mizutani, Y. Kawahito, S. Katayama, *Sci. Technol. Weld. Joining* **2013**, 15, 559.
- [32] J. Volpp, *Prod. Eng.* **2017**, 11, 9.
- [33] A. Heider, R. Weber, D. Herrmann, P. Herzog, T. Graf, *J. Laser Appl.* **2015**, 27, 22003.
- [34] L.-J. Zhang, G.-F. Zhang, J. Ning, X.-J. Zhang, J.-X. Zhang, *Mater. Des.* **2015**, 88, 720.
- [35] S. Mousavi, S. Niknejad, *Metall. Mater. Trans. A* **2009**, 40, 1469.
- [36] S. Mousavi, S. Niknejad, *J. Mater. Process. Technol.* **2010**, 210, 1472.
- [37] H.-C. Chen, G. Bi, M. Nai, J. Wei, *J. Mater. Process. Technol.* **2015**, 216, 287.

- [38] D.L. Reger, S.R. Goode, D.W. Ball, *Chemistry: Principles and practice*, Brooks/Cole, Cengage Learning, Belmont **2010**.
- [39] I.-H. Jung, P. Hudon, T. Vanderah, *J. Am. Ceram. Soc.* **2012**, 95, 3665.
- [40] W. Gale, T. Totemeier, *Smithells Metals Reference Book*, Elsevier, **2003**.
- [41] A. Hess, R. Schuster, A. Heider, R. Weber, T. Graf, *Phys. Procedia* **2011**, 12, 88.
- [42] M.A. Sommers, *Phosphorus*, Rosen Central, New York **2008**.

Received in final form: May 5<sup>th</sup> 2021